Multi-perspective heterodyne digital holography for high-speed imaging of density fluctuations in supersonic flow

R. Choudhary[1], W. Wang[1], C.M. Limbach[1,*]

1: Dept. of Aerospace Engineering, University of Michigan - Ann Arbor, USA
*Corresponding author: limbach@umich.edu

Keywords: interferometry, digital holography, high-speed imaging, tomography

ABSTRACT

Density fluctuation measurements with high spatio-temporal resolution provide meaningful insights into the dynamics of turbulent structures in shear layers, boundary layers, and disturbances that influence the transition to turbulence. The current contribution presents a new multiple perspective digital holographic imaging technique that aims to resolve high-frequency density fluctuations with spatial discrimination along the line of sight. A key element of the proposed method is the generation of a beamlet array of varying view angles that is spatially overlapped within the measurement zone. We present the first experimental realization of this approach using a 7-element hexagonally packed fly's eye lens array and analyze results for a pair of mutually perpendicular and axially offset sonic jets. The experimental apparatus also incorporates heterodyne detection with a heterodyne frequency set to $1/4$ of the imaging frame rate. The optical system performance is evaluated for a crossing jet flow and key design considerations for the multi-perspective optical system are discussed.

1. Introduction

The environment around supersonic and hypersonic flight vehicles is characterized by shock waves, compressible boundary layers, intense heating, and large fluctuations in pressure, velocity and temperature corresponding to thermomechanical loads on the vehicle. Laminar-turbulent transition of the boundary layer can further lead to a substantial, localized increase in skin friction drag and heat flux into the vehicle surface, which can significantly impact its performance, controllability, and integrity (Leyva, 2017). The likelihood and mechanisms of transition are influenced by the vehicle geometry, the nature of ambient disturbances, and freestream fluctuations of entropy and vorticity. (Schneider, 2015).

The problems of hypersonic boundary layer transition, as well as turbulent shock boundary layer interaction, have been the subject of intense experimental and computational studies often in the

context of canonical geometries (Vandomme et al., 2004; Franko & Lele, 2013; Sidharth et al., 2018; Ceruzzi et al., 2020; Reinert et al., 2020; Di Renzo & Urzay, 2021; Bae et al., 2023; Hao et al., 2022; Pehrson, Leonov, Melone, et al., 2023; Pehrson, Leonov, Miles, et al., 2023). However, it remains challenging to experimentally characterize these interactions simultaneously at the relevant sampling rates and locally in space. For this purpose, Focused Laser Differential Interferometry (FLDI) has been developed and applied to numerous investigations of transitioning flows and boundary layers. In this technique, the phase difference between two closely spaced laser beams is used to measure traveling density fluctuations. In particular the beam forming and focusing geometry is configured as a "nearly" common path interferometer which permits spatial localization of the measurement and rejection of out-of-plane disturbances (Parziale et al., 2013). Such measurements can be performed at extremely high rates, $\tilde{O}$(10 MHz), making them suitable for studying instabilities and transitioning flows (Ceruzzi et al., 2020; Gragston, Siddiqui, & Schmisseur, 2021). However, recent simulations have shown that FLDI can still be influenced by low wavenumber disturbances due to turbulent wall boundary layers (Benitez et al., 2022). Moreover, the accuracy of the measured FLDI data is contingent on the accuracy of the transfer function - and characteristic length scale - used for mapping phase measurements to density fluctuations. The assumptions underlying analytically derived transfer functions also depend on the nature of the flow itself (Lawson & Austin, 2023b,a). Recent efforts have extended the spatial sampling transverse to the optical axis using arrays of beamlets or beamlet pairs (Gragston, Price, et al., 2021) for multi-point measurements. This has been achieved by diffractive optics as well as microlens arrays (Marsh et al., 2024). Dispersion of the focusing optics has also been used to extend spatial sampling along the line of sight using a multi-wavelength approach (Benitez et al., 2023).

The present work aims to bridge the gap between discretely localized density fluctuation measurements by FLDI and quantitative full-field path-integrated techniques such as digital holography (Klee et al., 2021; Wilcox et al., 2019). In our approach, a fly's eye lens array is used to create a multiplexed interferometer array, with each beamlet corresponding to a unique view angle. Unlike FLDI, the beamlets are not focused, but they do significantly overlap during propagation through the measurement zone. In this way the imaging approach is more similar to focusing Schlieren (Weinstein, 1993; Weisberger & Bathel, 2022) but with a coherent light source. After passing through the interrogation region the beamlets are then interfered with a reference beam (local oscillator) and imaged by a conjugate lens array onto a high-speed camera, thereby producing a single multi-perspective interferogram. For this reason, we call the approach HiFleye, an abbreviation of High-speed Fly's eye imaging.

The present contribution describes the optical design and performance of the fly's eye imaging system and its initial application to an under-expanded jet. After providing a brief background in Section 2, we discuss design considerations and present the experimental configuration in Section 3. Results from the under-expanded jet are then presented in Section 4 followed by conclusions in Section 5.

2. Background

Like conventional digital holography and interferometry, the HiFleye technique produces measurements of phase based on interferograms. This section introduces the theory of digital holography and interferometry and in particular highlights the role of both spatial tilt and heterodyne detection implemented in the experimental apparatus.

2.1. Digital holography

HiFleye utilizes heterodyne digital holography to obtain path-integrated phase measurements, ϕ along several different lines of sight. The raw measurements consists of two dimensional interferograms, represented mathematically at each instant by a spatial variation of intensity at the detector/camera plane, I_i(x,y) which must be analyzed to obtain phase maps ϕ_i(x,y). Here, the subscript refers the *i*-th beamlet. The interferograms are produced by the interference of a reference beam electric field E_r and a probe beam electric field E_o at the detector plane, such that $E = E_o + E_i$, both beams being monochromatic. The intensity recorded on the camera I is then given by,

$$I = EE^* = |E_r|^2 + |E_o|^2 + E_o^* E_r + E_r^* E_o \tag{1}$$

$$\Rightarrow I = {a_r}^2 + {a_o}^2 + 2a_r a_o cos(\Delta\Phi). \tag{2}$$

Here, a_r and a_o represent the real amplitudes of the reference and probe wavefronts, while $\Delta\Phi = \Phi_o - \Phi_r$, where Φ_r and Φ_o represent the phase of the respective wavefronts. Notably, Φ_o contains the path integrated phase introduced by the unsteady flow field under investigation.

The phase difference can further be expanded to include both a spatial tilt, related to the direction mismatch between the object and reference beam wave vectors, and a frequency difference between the same:

$$\Delta\Phi(x, y, t) = (\vec{k_r} - \vec{k_o}) \cdot \vec{r} + (\omega_r - \omega_o)t + \phi_{abb}(x, y) + \Delta\phi(x, y, t). \tag{3}$$

The first term represents the contribution of tilt between the propagation vectors $\vec{k}$ of the reference and probe wavefronts while the second represents the contribution of frequency difference between the reference and the probe wavefronts. The third term represents the contribution of static higher order abberations present within the optical system. The fourth and final term is the quantity of interest and can be directly related to the density non-uniformities within the flow field.

More precisely, $\Delta\Phi(x, y, t)$ is derived from the path-integrated density of the flow-field,

$$\Delta\phi = \frac{2\pi}{\lambda} OPD = \frac{2\pi K_\lambda}{\lambda} \int_S (\rho(s) - \rho_0)\, ds, \tag{4}$$

where OPD is the optical path length difference introduced by the flow field along the line of sight S, λ is the wavelength of light and K_λ is the Gladstone-Dale Constant of the medium at the probing wavelength. In the following section we describe methods to obtain the phase $\Delta\phi$ from intensity measurements I which include spatial and temporal modulation in addition to static aberrations.

3. Experimental Details

3.1. Flow Facility

The flow field investigated in this work is generated by two mutually perpendicular, axially offset axisymmetric sonic jets. The vertical jet is oriented in the y-direction in our chosen coordinate system and supplied by dry, compressed air at 80 psi. The jet exits an orifice of diameter 0.29" into the ambient lab environment. The horizontal jet is oriented in the negative x direction in our coordinate system and exits a converging 0.05 inch diameter nozzle with a stagnation pressure of 120 psi. To support investigations of depth resolution, the jets are offset along the z-direction, which also serves as the optical axis, by 0.55 inches.

3.2. Optical Setup

A schematic of the experimental setup is shown in Figure 1. A $532nm$ single frequency laser (Equinox from MSquared Lasers) split by a 50/50 non-polarizing beamsplitter to produce the probe and reference beams. The reference beam is further routed through two acousto-optic frequency shifters (AA Optoelectronic Systems), the first driven at 110 MHz and the second driven at 110.0125 MHz. The $+1$ and -1 diffraction orders are used to obtain a final frequency shift of -12.5 kHz relative to the probe beam which is a quarter of the frame rate used in this study (50,000 fps). The camera consists of a Phantom TMX 5010 back-illuminated CMOS camera with 1280 $\times$ 800 pixel array. An exposure time of 0.1 μs was used in all experiments to minimize blurring due to flow motion. After frequency shifting, the reference beam is expanded $20\times$ by a pair of convex lenses and combined with the probe beam at a second beamsplitter.

Generating the multi-perspective beam array begins by passing the probe beam through a $20\times$ beam expander and illuminating a discrete lens array consisting of seven lenses ($f = 6$ cm, $D = 6$ mm). The lenses are mounted in a custom machined rigid polymer mount and arranged along

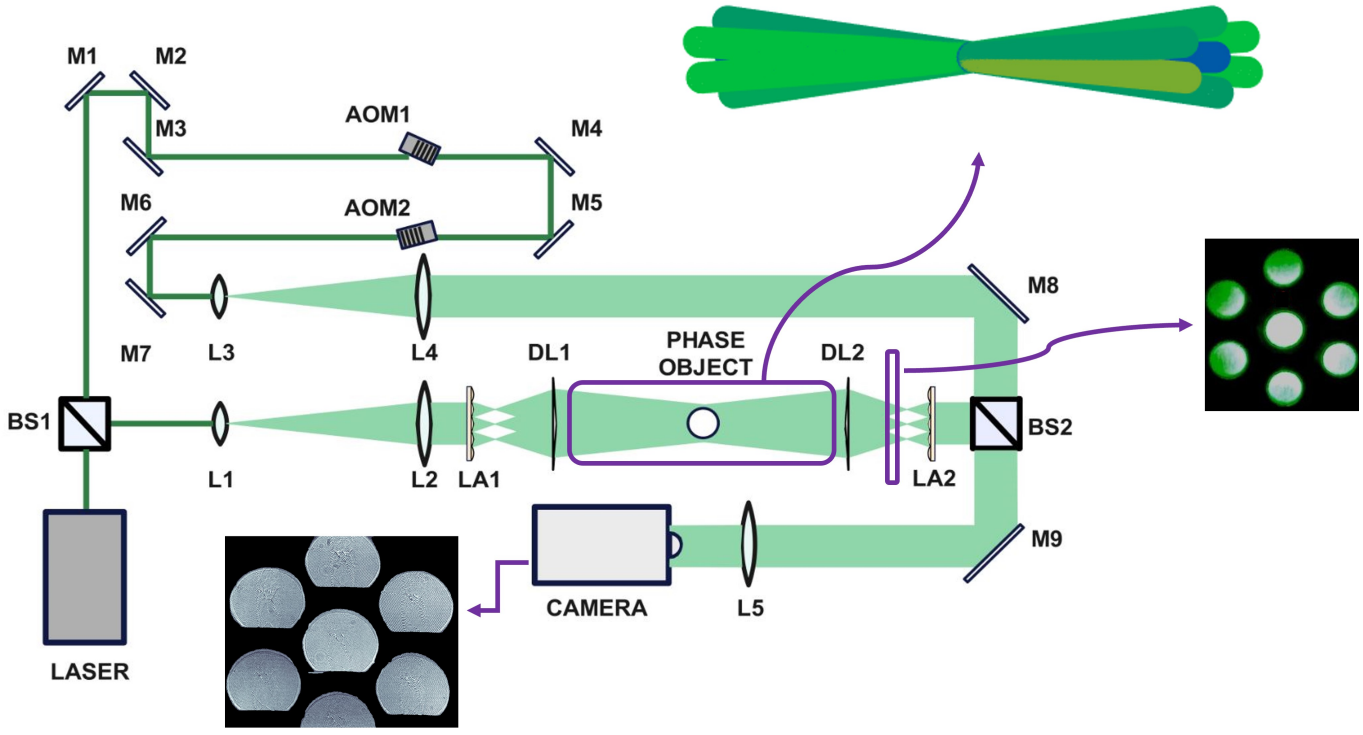

Figure 1. Schematic of the optical setup. Nomenclature: BS – Beam Splitter, L – Plano-convex Lens, DL – Doublet + Meniscus Lens, LA – Mini-Lens Array, M – Mirror, AOM – Acousto-Optic Modulator. (Inset - Top) Numerical simulation of the beamlets' trajectory. (Inset - Right) Beamlets generated by the lens array. The image was taken at a distance of $0.5f$ from the focal plane of the lens array. (Inset - Bottom) Raw interferograms recorded by the camera. Note that five of the seven beamlets are fully imaged by the camera for the selected magnification.

the vertices of a regular hexagon. Upon illumination by the expanded probe beam, the lens arrays lead to the formation of symmetrically oriented beamlets (see figure 2) which are collimated by a lens pair consisting of a meniscus lens ($f = 50$ cm) and a large aperture doublet lens ($f = 50$ cm). The lens pair combination was chosen to minimize the off-axis aberrations in collimated space. A crossing angle of approximately 9° at the measurement plane was achieved with this optical setup.

The optical arrangement enables probing the pair of sonic jets (phase object) through seven different perspectives, five of which were fully collected on the camera. Upon crossing the phase object, the beamlets are recollimated using a conjugate, identical imaging system. Notably, the conjugate discrete lens array is mounted in a 6-axis mount to obtain precise spatial and angular alignment and collimation of the beamlets. The interfered beamlets are finally imaged onto the camera sensor using a Keplerian telescope with a magnification of 0.8. Precise focusing of the imaging system was performed such as to minimize the shadowgraph effects in the interferograms. Irises were also used to prevent stray reflections from corrupting the measurement. The contrast of the fringe pattern was optimized by equalizing the amplitude of the probe and reference beams at the camera using neutral density filters.

Spatial calibration was performed using a transparent grid that was translated along the z-axis by a micrometer-driven translation stage. Images of the grid were recorded at 10 predetermined z stations with the reference beam blocked. The intersection points in the grid pattern served as collocation points in the coordinate system and were used to determine a point cloud from which ray propagation cosine angles were obtained for each pixel in the image data.

3.3. Phase Extraction

In most applications of holography and interferometry phase information must be derived from intensity measurements. To facilitate this process, it is advantageous to impose a temporal or spatial carrier frequency to help separate the phase term from the constant terms present in Eq. 2.1. The raw phase Φ must be further analyzed to determine the flow-induced phase change ϕ by removing the temporal and spatial modulation terms, $\Delta\vec{k} \cdot \vec{r}$ and $\Delta\omega t$, respectively.

For this purpose, two sets of measurements were taken during each experiment. Background interferograms, which include all terms in Eq. 2.1 except the flow-induced contribution, were recorded before each measurement. Following this, measurements were recorded with both jets flows present. Figures 2 & 3 show representative background and flow interferograms recorded for one beamlet.

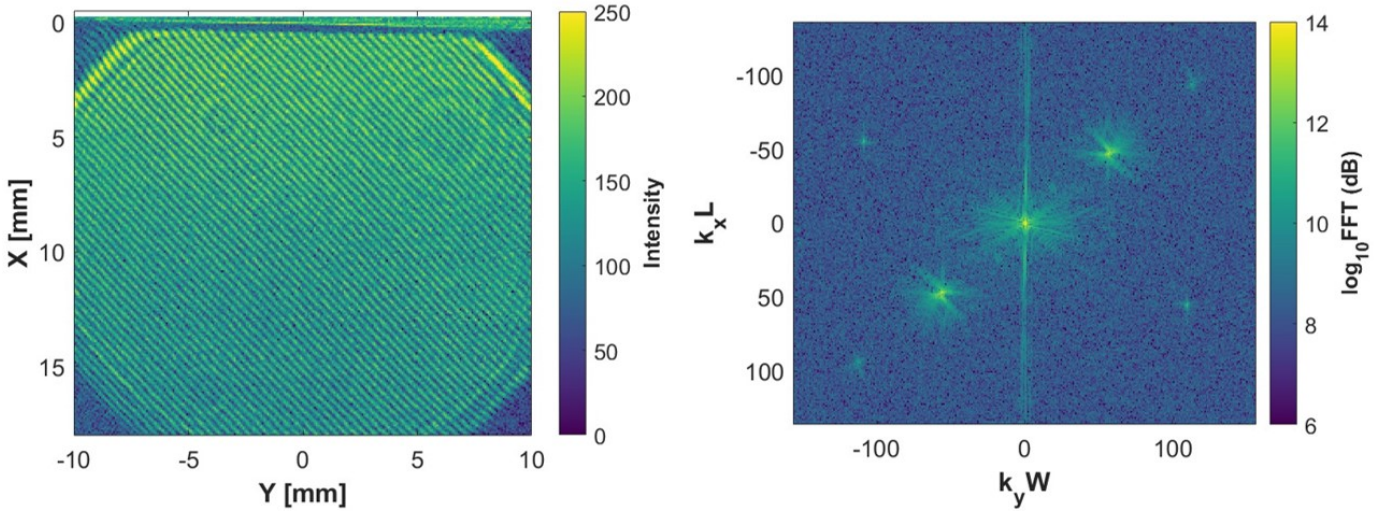

Figure 2. (Left) Interferogram obtained from beamlet 1 when there is no flow. (Right) 2D spatial FFT of the interferogram. The color map is plotted on a log scale.

In this work, the Fourier transform method for phase retrieval was adopted to recover the phase term for each beamlet (Goodman, 2005). In this approach, a large spatial tilt - ideally near a wavelength of 4 pixels - is imposed on image by deliberately misaligning the reference beam. In Fourier

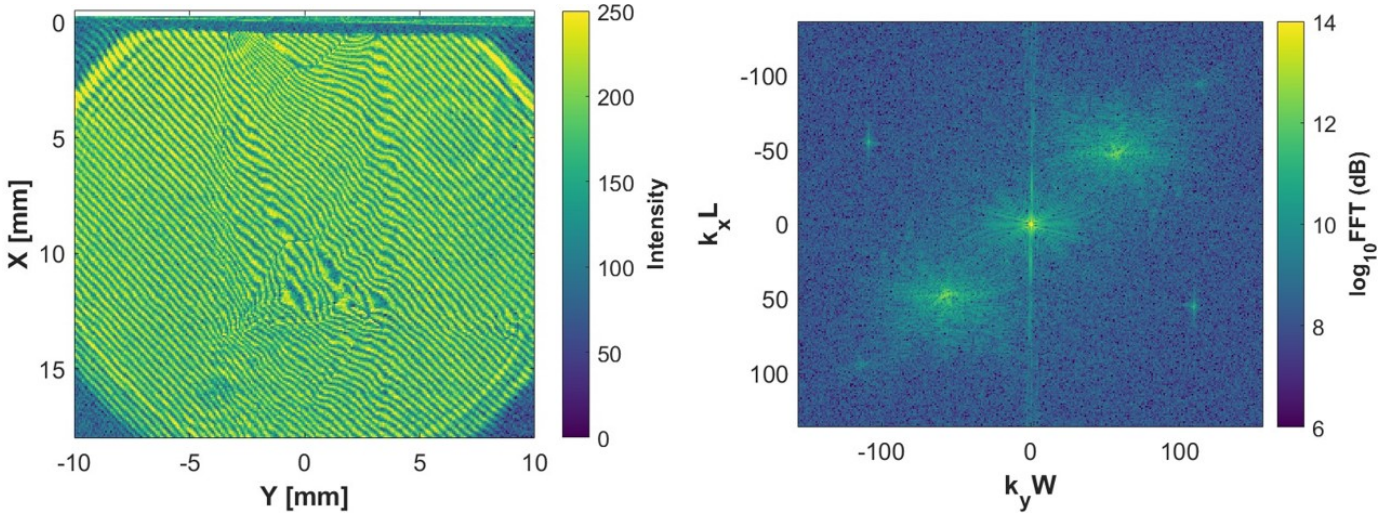

Figure 3. (Left) Interferogram obtained from beamlet 1 with both jets running. (Right) 2D spatial FFT of the interferogram. The color map is plotted on a log scale.

space, this shifts the phase data to $\pm\Delta\vec{k}$. In contrast, low-frequency intensity variations due to the beam profiles and vignetting are concentrated near zero spatial frequency, facilitating the filtering and rejection of noise. To extract the phase, data in the vicinity of $\pm\Delta\vec{k}$ was isolated using a rectangular region of interest, with regions outside being masked to zero. A 2D supergaussian filter function was also used to smoothly transition between the region of interest and the masked region. This process strongly suppresses contributions from the terms a_r and a_o in equation 2.1. The peak at $\pm\Delta\vec{k}$ is then recentered to zero frequency, removing the term $\Delta\vec{k}\cdot\vec{r}$ in the phase. Taking the complex argument of the inverse Fourier transform results in the phase term $\Phi - \Delta\vec{k}\cdot\vec{r}$ wrapped from $-\pi$ to π. Although temporal phase shifting, such as the common 4-point technique, could be implemented using this setup, analyzing such a scheme is left to future work. Here we only consider the Fourier phase retrieval method so as to maximize the temporal resolution of the jet flow experiments.

Spatial Fourier transforms of the interferograms are shown in Figures 2 & 3. The fringes in the background interferogram are inclined at nearly -45° resulting in two prominent peaks in the fourth and the second quadrant of the 2D Fourier transform. The peak at the origin represents the low spatial frequency components of the interferogram. The wrapped phase obtained from the Fourier analysis was unwrapped using the algorithm described in Ghiglia & Romero (1994). Both the wrapped and unwrapped phase maps from beamlet 1 are shown in the left and right panels of Fig.4. The contribution from the static background was then removed by subtracting the unwrapped phase obtained from the background calibration measurements. The phase mosaic produced by all five beams is shown in Fig.5. During the experiments, 80,000 frames were recorded in total at a frame rate of 50 kHz. Time averaged phase maps were calculated by averaging over the instantaneous unwrapped phase maps. Figure 6 shows a phase map obtained by

averaging over 12000 frames, and a root-mean-squared (RMS) phase obtained using the former as the mean.

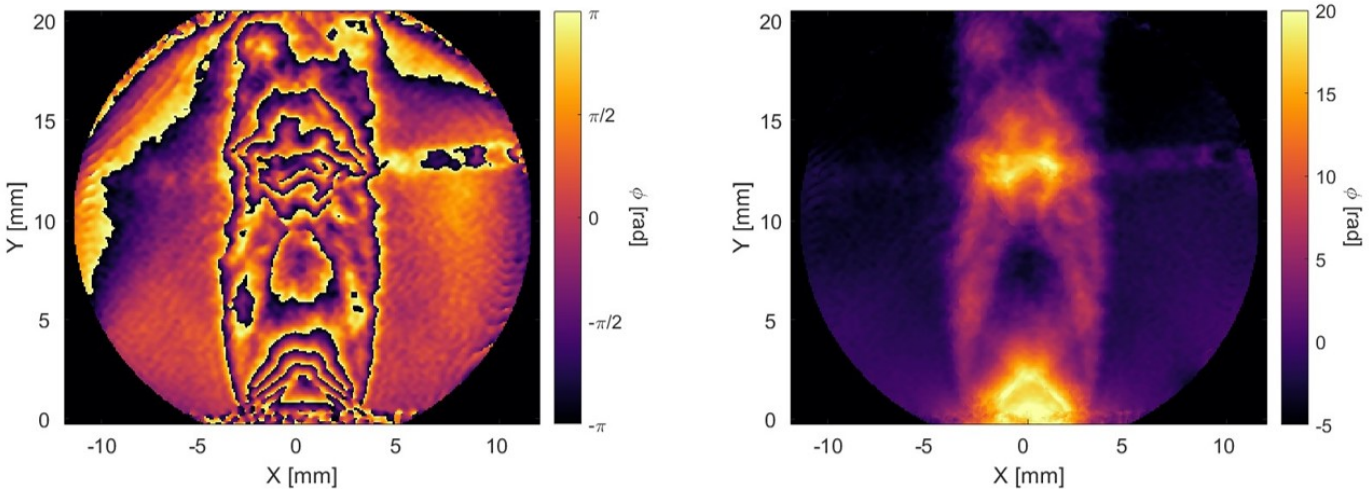

Figure 4. (Left) Wrapped phase recovered from the Fourier analysis. (Right) Instantaneous phase map obtained upon unwrapping the wrapped phase. The flow from the vertical orifice jet is from the bottom to the top while the flow from the horizontal nozzle jet is from the right to the left.

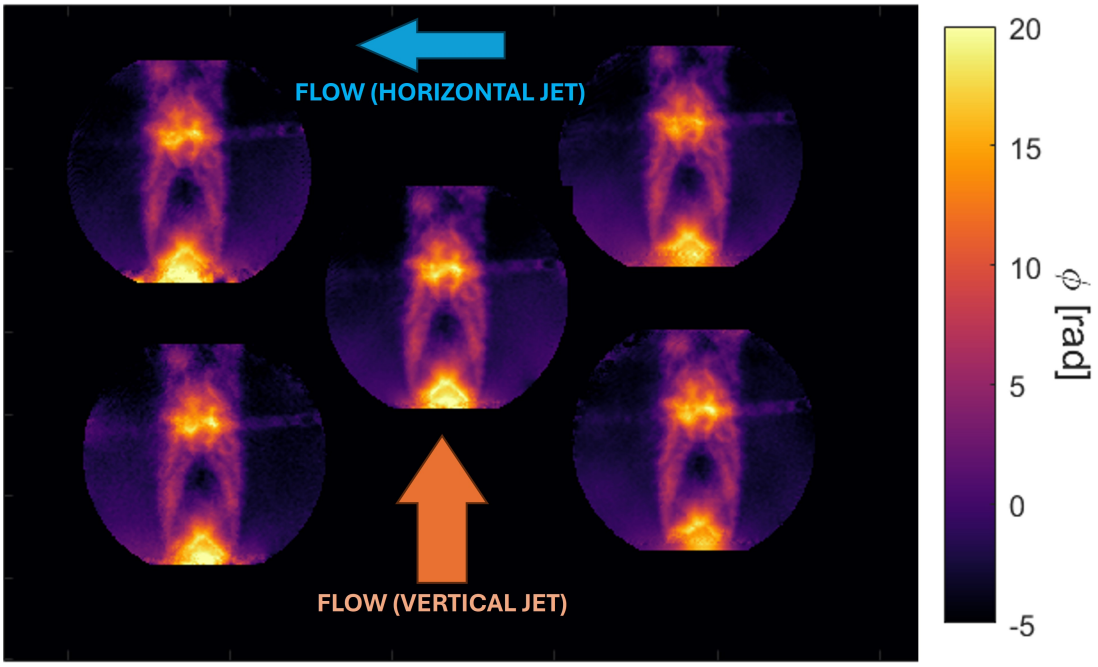

Figure 5. Instantaneous unwrapped phase maps obtained from five of the seven beamlets. The location of the phase maps corresponds to the relative physical location of the beamlets on the camera sensor. The arrows indicate the direction of air flow from both jets.

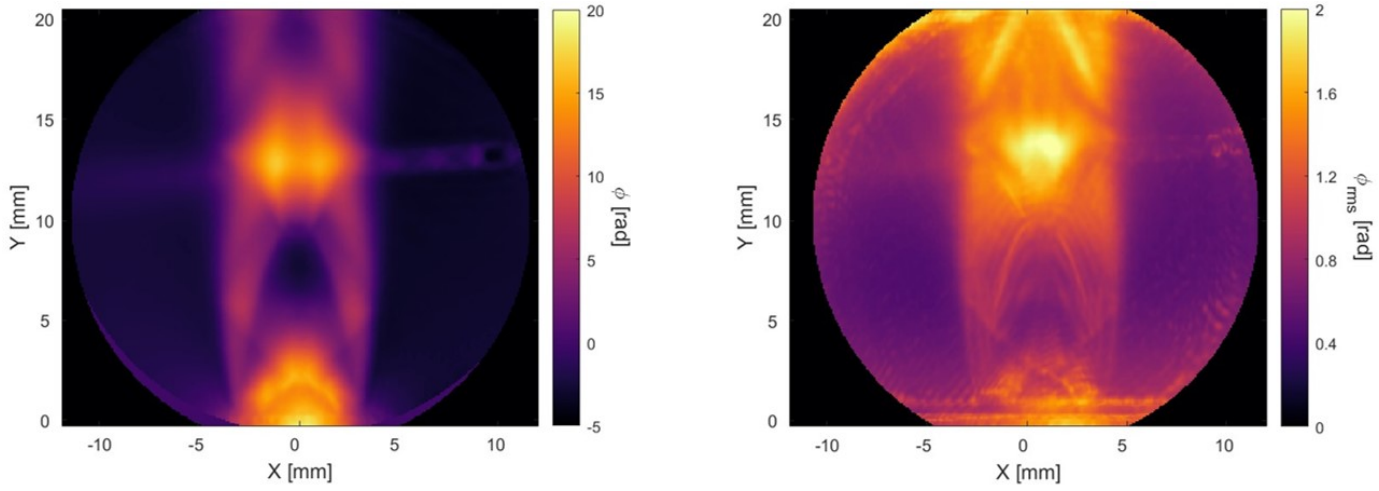

Figure 6. (Left) Time averaged phase map obtained by averaging over 12000 frames (240 ms). (Right) RMS phase map obtained from beamlet 1. Averaging was performed over 12000 frames.

4. Results & Discussion

Processed interferograms provide useful insights into the physics of the flow. This section discusses key features of the flow field and the impact of processing algorithms and the chosen optics on the resolution and uncertainty of the measurements.

4.1. Flow features

The instantaneous, time-averaged, and RMS phase maps provide insight into the dynamics of the shear layers and other disturbances in the flow. Since the phase is directly proportional to the path-integrated density, we can identify regions of compression and expansion by simply looking at the phase magnitude. In the plots, lower density corresponds to a negative phase shift while higher density corresponds to positive phase shift.

The fundamental structure of underexpanded jets are well known, and have been extensively studied experimentally (Franquet et al., 2015), primarily through Schlieren imaging. In these experiments the jet is highly under-expanded and the abrupt change in area near the exit leads to the formation of a characteristic barrel shock. Owing to the high upstream pressure, the flow reaches sonic velocity near the exit and expansion waves emanating from the nozzle edge cause the flow to expand. Interaction of expansion waves with the shear layer can be clearly observed from the phase maps. The boundary of the barrel shock is clearly discernible from the phase maps as is the Mach disc terminating the barrel shock. Although much smaller in magnitude, such features are also discernible in the horizontal jet. The RMS phase plot in Fig.6 also shows that the maximum fluctuation in the phase occurs downstream of the Mach disc.

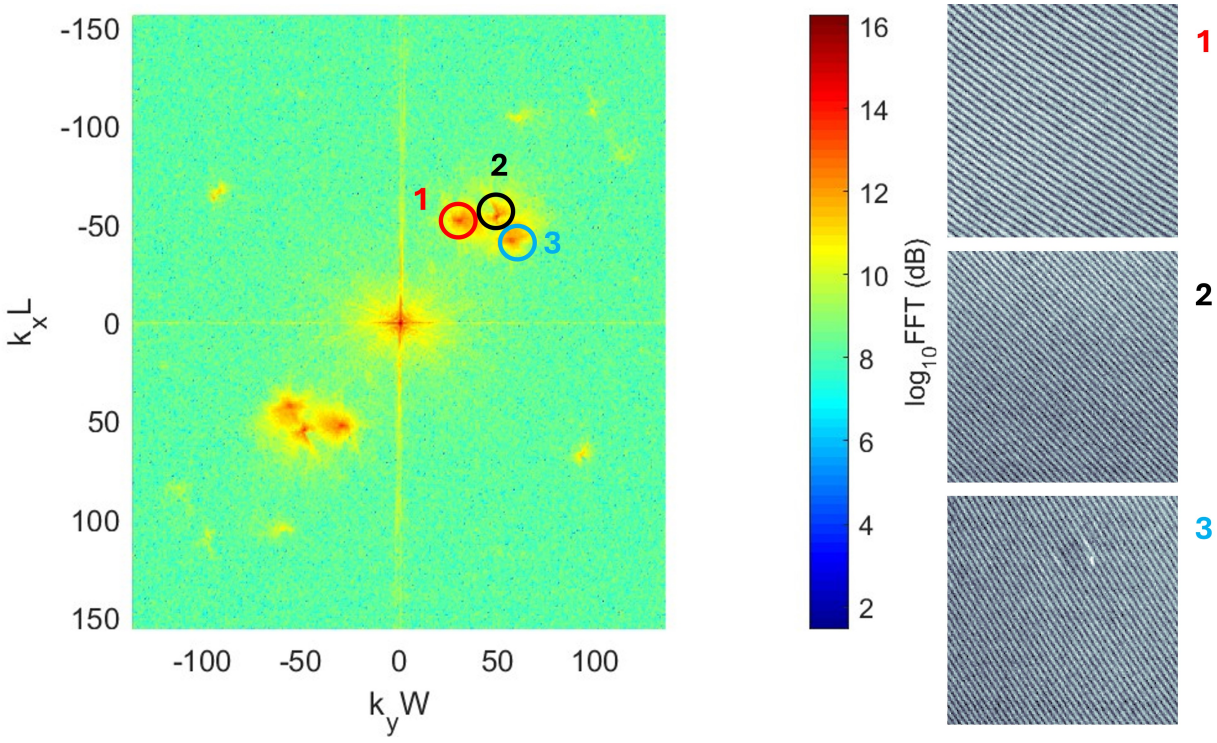

Figure 7. Superimposed 2D-FFT of interferograms obtained from three of the seven beamlets. The first order peaks are encircled, and corresponding interferograms are shown on the right.

4.2. Optical Parameter Trade-offs

In this section, we discuss three key trade-offs associated with the spatial and temporal resolution of HiFleye. The first trade-off is a associated with the number of view angles and rays. Since HiFleye uses a single camera to simultaneously image all beamlets, there is a natural degradation in the total number of available time-series phase measurements. The packing arrangement of lenses in the mini-lens array also influences the efficiency in utilization of the available sensor area. In the current setup, phase measurements are only obtained over 39% of the total 1.0 Mpix sensor due to the packing fraction of the lens array. Similarly, by dividing up the sensor into a number of beamlets, the image resolution is only 11% that available using the entire sensor. While this can be improved by reducing the number of beamlets, doing so will further reduce the number of independent view angles. In the context of future applications to tomography, the condition number of the forward projection matrix, A, will incur unacceptably large errors in tomographic reconstruction as the number of views decrease (Hämäläinen et al., 2014).

A second trade-off is associated with phase recovery from the measured interferograms and affects the spatial resolution and noise rejection in the extracted phase maps. In order to maximize the spatial resolution and effectiveness of spatial filtering, it is imperative to optimize the magnitude of the carrier frequency. Specifically, one aims to achieve a fringe spacing of exactly 4 pixels,

diagonally, to center the carrier frequency in one quadrant of the Fourier plane. This maximizes the spatial resolution of the inverted phase map and provides the greatest suppression of low frequency noise. To illustrate, the left panel of Fig. 7 shows the 2D-FFT of three of the seven beamlets. The first-order frequency peaks corresponding to each of the three beamlets are present at three distinct locations in the frequency space. The peak corresponding to beamlet 1 has the smallest distance from the origin while beamlet 2 has the largest. The corresponding fringes (shown in the right panel) are more closely spaced in beamlet 2. Note that any deviation from the ideal fringe spacing will lead to a reduction in spatial frequency of the phase map. Figure 7 also shows that the inclination of the fringes will not be uniform across all beamlets due to optical aberrations. Since the optical aberrations become more severe as the numerical aperture increases, larger crossing angles will eventually result in degraded spatial resolution. In the current HiFleye configuration, we achieve a maximum resolution of $112\mu m$ based on this limitation.

The final trade-off is between the temporal resolution of the diagnostic and the susceptibility of the measurements to temporally static/low-frequency noise. As mentioned in section 2, leveraging heterodyne interferometry provides us the capability to reject corruption from temporally static or low-frequency sources of noise. However, the algorithm adopted to achieve this involved a four-point phase shifting algorithm (described in section 3.3). The algorithm requires four consecutive frames. In essence, this degrades the temporal resolution of the diagnostic by a factor of four. While this might be an acceptable trade-off for flows with temporally stationary statistics, it may not be desirable for highly turbulent flows, or flows with a rapidly changing mean.

5. Conclusions

The development of a multi-perspective interferometric diagnostic, HiFleye, for ultra-fast volumetric imaging of high-frequency density fluctuations in high-speed flows is reported. The diagnostic involves the generation of an array of probe beams which interrogate the flow field of interest through different view angles which then undergo interference with a reference beam. The experimental setup for realizing this diagnostic was discussed and measurements of path integrated phase in a flow field consisting of two mutually orthogonal sonic underexpanded jets were presented. The diagnostic enabled high-quality measurement of two-dimensional path integrated phase fields from five view angles. The diagnostic also enabled the fastest ever interferometric measurement of 2D density fields in compressible, high-speed flows. Successful accomplishment of simultaneous high-speed multi-perspective interferometry has provided the foundation for the extension of this diagnostic to perform tomography.

Acknowledgements

This work has been supported by the Air Force Office of Scientific Research under grant FA9550-20-1-0251 overseenby Dr. Sarah Popkin.

Nomenclature

$FLDI$	Focused Laser Differential Interferometry
I	Intensity
ϕ	Flow-induced phase
E	Complex electric field amplitude
a	Real amplitude of the wavefront
$\Delta\Phi$	Total phase difference
$\vec{k}$	Propagation vector
$\vec{r}$	Position vector
ω	Angular frequency of the wavefront
ϕ_{abb}	Phase shift due to aberrations
f_{het}	Heterodyne frequency
ρ	Density
λ	Wavelength
OPD	Optical Path Difference
K_λ	Gladstone-Dale constant
f	Focal length
D	Diameter
FFT	Fast Fourier Transform
$\Delta\vec{k}$	Spatial tilt wave vector

References

Bae, H., Lim, J., Kim, M., & Jee, S. (2023). Direct-numerical simulation with the stability theory for turbulent transition in hypersonic boundary layer. *International Journal of Aeronautical and Space Sciences*, *24*(4), 1004–1014.

Benitez, E. K., Borg, M. P., Hill, J. L., Aultman, M. T., Duan, L., Running, C. L., & Jewell, J. S. (2022). Quantitative focused laser differential interferometry with hypersonic turbulent boundary layers. *Applied Optics*, *61*(31), 9203–9216.

Benitez, E. K., Borg, M. P., Rhodes, C., & Jewell, J. S. (2023). Optical-axis spatial sensitivity of a simulated focused laser differential interferometer. *AIAA Journal*, *61*(5), 1925–1938.

Ceruzzi, A., Callis, B., Weber, D., & Cadou, C. P. (2020). Application of focused laser differential interferometry (fldi) in a supersonic boundary layer. In *Aiaa scitech 2020 forum* (p. 1973).

Di Renzo, M., & Urzay, J. (2021). Direct numerical simulation of a hypersonic transitional boundary layer at suborbital enthalpies. *Journal of Fluid Mechanics*, *912*, A29.

Franko, K. J., & Lele, S. K. (2013). Breakdown mechanisms and heat transfer overshoot in hypersonic zero pressure gradient boundary layers. *Journal of Fluid Mechanics*, *730*, 491–532.

Franquet, E., Perrier, V., Gibout, S., & Bruel, P. (2015). Free underexpanded jets in a quiescent medium: A review. *Progress in Aerospace Sciences*, *77*, 25–53.

Ghiglia, D. C., & Romero, L. A. (1994). Robust two-dimensional weighted and unweighted phase unwrapping that uses fast transforms and iterative methods. *JOSA A*, *11*(1), 107–117.

Goodman, J. W. (2005). *Introduction to fourier optics*. Roberts and Company publishers.

Gragston, M., Price, T. J., Davenport, K., Schmisseur, J. D., & Zhang, Z. (2021). An m by n fldi array for single-shot multipoint disturbance measurements in high-speed flows. In *Aiaa scitech 2021 forum* (p. 0599).

Gragston, M., Siddiqui, F., & Schmisseur, J. D. (2021). Detection of second-mode instabilities on a flared cone in mach 6 quiet flow with linear array focused laser differential interferometry. *Experiments in Fluids*, *62*, 1–12.

Hämäläinen, K., Harhanen, L., Hauptmann, A., Kallonen, A., Niemi, E., & Siltanen, S. (2014). Total variation regularization for large-scale x-ray tomography. *Int. J. Tomogr. Simul*, *25*(1), 1–25.

Hao, J., Fan, J., Cao, S., & Wen, C.-Y. (2022). Three-dimensionality of hypersonic laminar flow over a double cone. *Journal of Fluid Mechanics*, *935*, A8.

Klee, A., Thurman, S. T., & Alley, T. (2021). Digital holographic tomography for path-resolved turbulence measurements. In *Unconventional imaging and adaptive optics 2021* (Vol. 11836, pp. 125–136).

Lawson, J. M., & Austin, J. M. (2023a). Recovering density disturbance spectra from fldi. part 1. *Applied Optics*, *62*(12), 3042–3053.

Lawson, J. M., & Austin, J. M. (2023b). Recovering density disturbance spectra from fldi. part 2: comparisons with previous methods. *Applied Optics*, *62*(12), 3054–3061.

Leyva, I. A. (2017). The relentless pursuit of hypersonic flight. *Physics Today*, *70*(11), 30–36.

Marsh, A. W., Kramer, A. N., Maranto, K. N., & Mazumdar, Y. C. (2024). Imaging focused laser differential interferometry. *Optics Letters*, *49*(8), 2109–2112.

Parziale, N., Shepherd, J., & Hornung, H. (2013). Differential interferometric measurement of instability in a hypervelocity boundary layer. *AIAA journal*, *51*(3), 750–754.

Pehrson, J. C., Leonov, B. S., Melone, K., Lakebrink, M. T., Bowersox, R., Miles, R. B., & Limbach, C. M. (2023). Hypersonic fleet velocimetry and uncertainty characterization in a tripped boundary layer. *Measurement Science and Technology*, *35*(1), 015206.

Pehrson, J. C., Leonov, B. S., Miles, R. B., Lakebrink, M. T., & Limbach, C. (2023). Wall-normal fleet velocimetry in a canonical hypersonic inlet. In *Aiaa scitech 2023 forum* (p. 0220).

Reinert, J. D., Candler, G. V., & Komives, J. R. (2020). Simulations of unsteady three-dimensional hypersonic double-wedge flow experiments. *AIAA journal*, *58*(9), 4055–4067.

Schneider, S. P. (2015). Developing mechanism-based methods for estimating hypersonic boundary-layer transition in flight: The role of quiet tunnels. *Progress in Aerospace Sciences*, *72*, 17–29.

Sidharth, G., Dwivedi, A., Candler, G. V., & Nichols, J. W. (2018). Onset of three-dimensionality in supersonic flow over a slender double wedge. *Physical Review Fluids*, *3*(9), 093901.

Vandomme, L., Chanetz, B., Benay, R., & Perraud, J. (2004). Transitional shock wave boundary layer interactions in hypersonic flow at mach 5. *ONERA, TP no. 2004-11*, *2004*(11).

Weinstein, L. M. (1993). Large-field high-brightness focusing schlieren system. *AIAA journal*, *31*(7), 1250–1255.

Weisberger, J. M., & Bathel, B. F. (2022). Single source/cutoff grid, self-aligned focusing schlieren system. *Experiments in Fluids*, *63*(1), 38.

Wilcox, C. C., Radosevich, C. J., Healy, K. P., Tuffli, A. L., Agena, B. D., Spencer, M. F., & Wittich III, D. J. (2019). Digital holography wavefront sensing with a supersonic wind tunnel. *Holography: Advances and Modern Trends VI*, *11030*, 110–119.